remote sensing

MDPI

Article

Three-Dimensional Structure Inversion of Buildings with Nonparametric Iterative Adaptive Approach Using SAR Tomography

Xing Peng [1,2], Changcheng Wang [1,3], Xinwu Li [2,*], Yanan Du [4], Haiqiang Fu [1], Zefa Yang [1] and Qinghua Xie [5]

1 School of Geosciences and Info-Physics, Central South University, Changsha 410083, China; hubeipx@csu.edu.cn (X.P.); wangchangcheng@csu.edu.cn (C.W.); haiqiangfu@csu.edu.cn (H.F.); yangzf@csu.edu.cn (Z.Y.)
2 Key Lab of Digital Earth Sciences, Institute of Remote Sensing & Digital Earth, Chinese Academy of Sciences, Beijing 100094, China
3 Key Laboratory of Metallogenic Prediction of Nonferrous Metals and Geological Environment Monitoring, Ministry of Education, Central South University, Changsha 410083, China
4 School of Geographical Sciences, Guangzhou University, Guangzhou 510006, China; yndu@gzhu.edu.cn
5 Faculty of Information Engineering, China University of Geoscience (Wuhan), Wuhan 430074, China; xieqh@cug.edu.cn
* Correspondence: lixw@radi.ac.cn

Received: 20 May 2018; Accepted: 20 June 2018; Published: 25 June 2018



Abstract: Synthetic aperture radar tomography (TomoSAR) is a useful tool for retrieving the three-dimensional structure of buildings in urban areas, especially for datasets with a high spatial resolution. However, among the previous TomoSAR estimators, some cannot retrieve the 3-D structure of objects with a high elevation resolution, some cannot maintain the spatial resolution, and some require the selection of a hyperparameter. To overcome these limitations, this paper proposes a new nonparametric iterative adaptive approach with a model selection tool based on the Bayesian information criterion (IAA-BIC) for the application of TomoSAR in urban areas. IAA-BIC employs weighted least squares to acquire a high elevation resolution and works well for both distributed and coherent scatterers, even with single-look. Concurrently, IAA-BIC does not require the user to make any difficult selection regarding a hyperparameter. The proposed IAA-BIC estimator was tested in simulated experiments, and the results confirmed the advantages of the IAA-BIC estimator. Moreover, the three-dimensional structure of the Hubei Science and Technology Venture building in Wuhan, China, was retrieved through the IAA-BIC method with nine very high spatial resolution TerraSAR-X images. The height estimation accuracy for this building was about 1% and 4% relative to its real height for single-look and multi-look, respectively. In addition, a comparison between the IAA-BIC estimator and some of the typical existing TomoSAR estimators (Capon, MUSIC, and compressed sensing (CS)) was also carried out. The results indicate that the IAA-BIC estimator obtains a better resolution for coherent sources than Capon and MUSIC; notably, the IAA-BIC estimator obtains a similar performance to CS, but in less computation time.

Keywords: IAA; IAA-BIC; SAR tomography (TomoSAR); urban areas; three-dimensional structure

1. Introduction

Recently, the launch of a new generation of SAR satellites (e.g., TerraSAR-X, TanDEM-X, and COSMO-SkyMed) has provided us with many high spatial resolution SAR datasets [1–3]. This offers an unprecedented chance to identify and model three-dimensional (3-D) urban infrastructures

(e.g., structure, shape, and texture), owing to the weather-independent characteristics of the SAR sensors. However, due to the side-looking imaging geometry, the severe layover and foreshortening effects impede the 3-D infrastructure modeling in urban areas when using the classical interferometric SAR (InSAR) techniques [4].

The synthetic aperture radar tomography (TomoSAR) technique has been confirmed as a useful and advanced tool to solve this problem, given its ability in three-dimensional imaging [5–7]. Notably, the TomoSAR synthesizes an additional aperture along the elevation direction through a combination of multi-baseline acquisitions, in addition to the formation of the conventional aperture in the azimuth-range plane. Therefore, TomoSAR can separate different scatterers in one resolution cell; accordingly, it is theoretically capable of retrieving the 3-D structure of objects, even for cells affected by layover and foreshortening.

To date, various spectral analysis methods have been developed for TomoSAR to perform tomography inversion. These methods can be divided into three groups: (1) nonparametric spectral estimation [8–13], (2) parametric spectral estimation [14–20], and (3) the compressive sensing (CS) approach [21–32]. Each of the three groups of TomoSAR methods have their respective advantages and drawbacks. For instance, the nonparametric spectral estimators (e.g., beamforming [8,12] and Capon [9,12]) are robust to focusing artifacts but obtain a low elevation resolution. The parametric spectral estimators, such as multiple signal classification (MUSIC) estimator [14], the maximum likelihood (ML) estimators [15], and the weighted subspace fitting (WSF) estimators [15,16], can obtain a better elevation resolution than the nonparametric spectral estimators. On the other hand, they do require some prior information input, such as the number of scatterers, resulting in their sensitivity to the model error. Moreover, multi-look is required to estimate the sample variance matrix in most of the nonparametric and parametric spectral estimators, degrading the spatial resolution of the inversed 3-D structure map in both the azimuth and slant-range directions. It is important to maintain the azimuth-range resolution to observe the inherent scale of urban infrastructures, especially for high spatial resolution SAR images. In addition, coherent scatterers are frequently encountered in urban areas, and some estimators such as Capon and MUSIC show degraded performances in the case of coherent sources [15,16]. The compressed sensing (CS) method can achieve super-resolution along the elevation direction without any prior information and can maintain the spatial resolution with single-look. However, it requires the user to select the hyperparameter, which directly affects the performance of CS. If this value is too small, it can lead to overfitting, whereas too large of a value can lead to underfitting. In practice, the user needs to adjust this value repeatedly until a good performance is obtained, which can be time intensive. In summary, the aforementioned estimators are not hyperparameter-free and cannot retrieve the 3-D structure of objects with a high elevation resolution while simultaneously maintaining the spatial resolution.

To overcome the above-mentioned limitations of the existing TomoSAR estimators, we propose a new nonparametric iterative adaptive approach (IAA) with a model selection tool based on the Bayesian information criterion (BIC) to retrieve the 3-D structure of urban infrastructures, which is referred to as IAA-BIC. IAA-BIC is the post-processing result of IAA through the use of the BIC-based model-order selection tool to remove spurious, insignificant estimations. The proposed IAA-BIC method offers several benefits that the existing TomoSAR estimators cannot provide. Firstly, it can estimate the power of the reflectivity along the elevation direction without requiring any prior knowledge by the weighted least squares approach [33,34]. Secondly, the IAA method performs well for both distributed and coherent scatterers with either a few multiple looks or single-look, which can maintain the spatial resolution. Thirdly, the IAA-BIC estimator can give sparse point detection results, without requiring any difficult selection of hyperparameter.

The aim of this study is to provide a hyperparameter-free sparse spectral estimation method which offers high elevation resolution power as well as maintains the spatial resolution for the application of TomoSAR over urban areas.

2. Methodology

2.1. Overview of the TomoSAR Imaging Model

Through multiple baseline observations of SAR over the same area at different times and slightly different incidence angles, a stack of N SAR images can be obtained. For the nth image after co-registration, deramping, and phase calibration with respect to a common master image, the focused complex value $y_n(l)$ at an arbitrary pixel (x_0, y_0) can be expressed as [6]:

$$y_n(l) = \int \gamma_s(l) \exp(-j2\pi\xi_n s) ds \tag{1}$$

where $l = 1, \cdots, L$ indicates one of the L independent realizations of the signal acquisition. In other words, L equates the number of looks. $\gamma_s(l)$ represents the complex reflectivity along the elevation direction s, and j is the plural unit. ξ_n is the spatial frequency, which depends on the perpendicular baseline b_n, the slant range between the master image and the pixel r, and the wavelength λ, and is written as:

$$\xi_n = \frac{-2b_n}{\lambda r} \tag{2}$$

The continuous-space system model of (1) shows that the multi-baseline acquisitions can be regarded as a randomly sampled Fourier transform of $\gamma_s(l)$. Thus, we can define $\rho_s = \frac{\lambda r}{2\Delta b}$ as an inherent Rayleigh resolution for the elevation, where Δb is the total baseline span [6,19].

By discretizing the continuous reflectivity $\gamma_s(l)$ with D intervals along the elevation s, the system model (1) can be approximately written as [6]:

$$y(l) = Ax(l) + e(l) \tag{3}$$

where $y(l)$ is the vector of the N observation measurements; $x(l)$ is the unknown discrete reflectivity vector with D elements with $x_d(l) = \gamma_{s_d}(l)$ and $s_d (d = 1, \cdots, D)$ represent the discrete height position; $e(l)$ is the noise vector that contains N elements; and A is named an $N \times D$ steering matrix with $A = [a(s_1), \cdots, a(s_D))]$. The steering vector $a(s_d)$ is given by:

$$a(s_d) = [\exp(-j2\pi\xi_1 s_d), \cdots, \exp(-j2\pi\xi_N s_d)]^T \tag{4}$$

where $(\cdot)^T$ represents the transpose operator of a vector or a matrix.

If K scatterers existed in one resolution cell, their elevation positions could be estimated through detecting the coordinates of K largest local maxima of the reflectivity power, expressed as follows [16]:

$$s_k = argmax_{s,loc} \left\{ \frac{1}{L} \sum_{l=1}^{L} |x_d(l)|^2 \right\}_{d=1}^{D} (k = 1, \cdots, K) \tag{5}$$

We can then obtain the vertical height h_k perpendicular to the horizontal plane by a simple transformation factor, as follows:

$$h_k = s_k \times sin\theta \tag{6}$$

where θ is the incidence angle of the radar.

2.2. IAA-BIC TomoSAR Method

In urban areas, there are usually a few scatterers inside one resolution cell, which is much less than the discrete interval number along the vertical direction (that is, $K << D$). As a result, the complex reflectivity coefficients can be considered as a sparse source along the elevation. Thus, we propose the IAA-BIC TomoSAR method. IAA-BIC consists of two steps [33]. We first apply the IAA algorithm to

obtain the reflectivity estimation. We then use the model-order selection tool, which is based on BIC, to remove spurious, insignificant estimations, obtaining the final result.

Let P be a $D \times D$ diagonal matrix, whose diagonal contains the power of reflectivity at each elevation location. The dth diagonal element p_d can be expressed as:

$$p_d = \frac{1}{L}\sum_{l=1}^{L}|x_d(l)|^2 \tag{7}$$

From Equation (5), it is found that the diagonal elements of the weight matrix P are the parameters of interest.

For the TomoSAR imaging model (3), the covariance matrix of $y(l)$ can be given by:

$$R = E(y(l)y^*(l)) \triangleq APA^* \tag{8}$$

where $E(\cdot)$ is the expectation operator; and $(\cdot)^*$ represents the conjugate transpose operator of a vector or a matrix.

IAA is a nonparametric iterative adaptive algorithm based on the weighted least squares (WLS) approach [33,34]. The WLS cost function of Equation (3) is given by:

$$f = \sum_{l=1}^{L}\|y(l) - x_d(l)a_d\|^2_{Q_d^{-1}} \tag{9}$$

where $\|z\|^2_{Q_d^{-1}} \triangleq z^*Q_d^{-1}z$. Q_d is the noise covariance matrix, which can be defined as:

$$Q_d = R - p_d a_d a_d^* \tag{10}$$

where $a_d = a(s_d)$, is the dth column vector of steering matrix A.

Minimizing (9) with respect to $x_d(l)$ yields:

$$x_d(l) = \frac{a_d^*Q_d^{-1}y(l)}{a_d^*Q_d^{-1}a_d} \tag{11}$$

Using (10) and the matrix inversion lemma, the above equation can be written as:

$$x_d(l) = \frac{a_d^*R^{-1}y(l)}{a_d^*R^{-1}a_d} \tag{12}$$

By inspecting (7), (8) and (12), parameter $x_d(l)$ needs the covariance matrix R, the covariance matrix R depends on the weight matrix P and the weight matrix P also requires parameter $x_d(l)$. Accordingly, this approach must operate in an iterative way.

Omitting the iteration index for simplicity, the Equation (12) can be rewritten as [34]:

$$x_d(l) = w_d y(l);\ w_d = \frac{a_d^*R^{-1}}{a_d^*R^{-1}a_d} \tag{13}$$

Then, the diagonal element p_d of the weight matrix P can be rewritten as [34]:

$$p_d = w_d\hat{R}w_d^* \tag{14}$$

where $\hat{R} = \frac{1}{L}\sum_{l=1}^{L}y(l)y(l)^*$, is the sample covariance matrix.

Thus, the iterative process can be also carried out as "Iteration" in Figure 1. The "convergence" in Figure 1 means $\|P^{current} - P^{previous}\|/\|P^{previous}\| \leq 10^{-4}$, indicating that the iteration process is terminated when the current estimates of P for the last two iterations remain almost constant. From

Equation (5), it is found that the scatterers positions depend on the reflectivity power estimations. During the iterative process, there is no need to estimate the scatterers positions and they can be directly obtained from the final results of powers.

Model-order selection [35–37], which is based on Information Theoretic Criteria (ITC), is a useful tool to clean the estimation of spurious, insignificant scatterers, giving the most likely number of point scatterers along the elevation inside an azimuth-range pixel [18,24]. Furthermore, BIC [36,38,39] has been demonstrated to be one of the best penalized likelihood criteria for model-order selection schemes in tomographic applications [19]. Accordingly, we incorporated a model-order selection tool, which is based on BIC, into the IAA algorithm, obtaining the sparse estimation without requiring any difficult selection of hyperparameter.

Let Ω denote a set that contains the peak indices of the reflectivity power $\{p_d\}_{d=1}^{D}$ and Γ denotes the set of the peak indices selected by the BIC algorithm so far.

The IAA-BIC algorithm works as shown in Figure 1:

(1) The parameters $x(l)$ and P are estimated from the IAA algorithm.
(2) Detect all peaks of the reflectivity power and put their indices into Ω. Initializes Γ as an empty set $\varnothing$.
(3) The first peak is selected from the set Ω according to the minimum BIC value and put its index into Γ.
(4) The ith peak, from the set $\Omega - \Gamma$, which, together with the selected peaks, gives the minimum BIC, is determined and so on until the BIC value does not decrease anymore. Throughout the loop, keep updating Γ by putting the index of the selected peak.
(5) The selected peak indices and their corresponding reflectivity power are the final estimated results.

The BIC value is calculated as follows [35,38]:

$$BIC_i(\eta) = 2NL \ln \left(\sum_{l=1}^{L} \left\| y(l) - \sum_{j \in \{\Gamma \cup i\}} a_j x_j(l) \right\|_2^2 \right) + 3\eta \ln (2NL) \tag{15}$$

where $\eta = |\Gamma| + 1$, and $|\Gamma|$ denotes the size of the set Γ, i is the index of the current peak under consideration. $\{x_j(l)\}_{l=1}^{L}$ is the reflectivity estimate corresponding to elevation position s_j, $j \in \{\Gamma \cup i\}$.

Finally, after obtaining final reflectivity power estimation, we can calculate the scatterers' elevation positions through Equation (5).

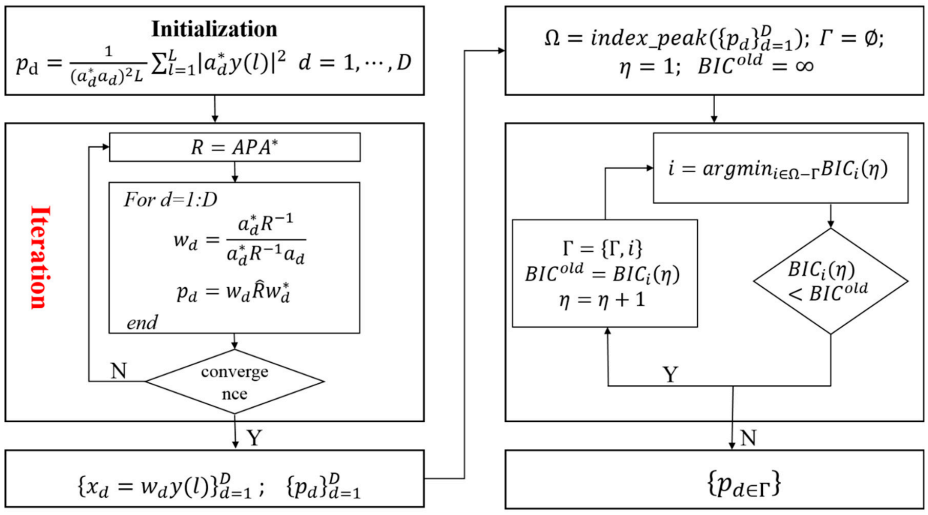

Figure 1. Details of the IAA-BIC TomoSAR method.

3. Numerical Examples

On the basis of the acquisition parameters described in Section 4 (see Table 1 and Figure 5), simulated experiments were performed to investigate the advantages of the proposed approach.

Distributed scatterers are characterized by a scattering response with a random behavior that is disturbed by the speckle. For coherent scatterers, the backscattering signal is roughly stable over all the observations [14–16]. According to the aforementioned statistical information, a hybrid signal was assumed, including two distributed scatterers whose heights were 0 m and 15 m, respectively, and two deterministic scatterers located at 5 m and 10 m. The tomographic inversion was carried out in the different simulated experiments on the extent of the elevation profile.

(1) Considering that the classical spectral estimators (Capon and MUSIC) are only suitable for multi-look, a comparison of the reconstruction performance between IAA-BIC and the classical spectral estimators (Capon and MUSIC) is presented for a simulated signal with 25 looks.
(2) In urban areas, CS is generally applied with single-look, maintaining the spatial resolution. Thus, a comparison of the reconstruction performance between IAA-BIC and CS is presented for a simulated signal with single-look.

On the basis of the above simulations, some observations can be made.

(1) For the profile reconstruction with multi-look (L = 25), the Capon algorithm clearly detected the two distributed scatterers, but failed to discriminate the two coherent scatterers (see Figure 3a). This situation was also seen in the performance of MUSIC. Although MUSIC obtained a higher elevation resolution and less sidelobe than Capon, it also could not detect the two coherent scatterers (see Figure 3b). However, the IAA-BIC estimator succeeded in recognizing these four scatterers (see Figure 3c). This suggests that IAA-BIC can work well for both distributed and coherent sources, but both Capon and MUSIC showed a degraded performance in the case of coherent sources.
(2) For the sparse profile reconstruction with single-look (see Figure 2), IAA-BIC obtained the height of the four scatterers accurately, without requiring any selection of hyperparameter. This shows that IAA-BIC can obtain a reliable sparse estimation, even with single-look. As for the CS method, its performance depends on the hyperparameter. If this value is not suitable, there will be sidelobes (three red circles in Figure 2b) as well as some elevation estimation bias (two green circles in Figure 2b). When the hyperparameter is appropriate, CS can discriminate the scatterers with a high elevation resolution (as can be seen in Figure 2c). This means that CS requires us to adjust the hyperparameter repeatedly until it obtains a good performance, leading to a high time investment. In this study, the CVX solver [40] was used to solve the $L1$-norm minimization for the CS estimator, thanks to its ease of implementation and compactness.
(3) According to Figures 3c and 2a, the IAA-BIC estimator can work well for both multi-look and single-look. It is important to maintain the azimuth-range resolution to observe the inherent scale of urban infrastructures, especially for high spatial resolution SAR images. However, in practice, multi-look, which involves averaging pixels in the azimuth and/or range directions, reduces the spatial (azimuth-range) resolution. This is an inappropriate way for the application of TomoSAR over urban areas.

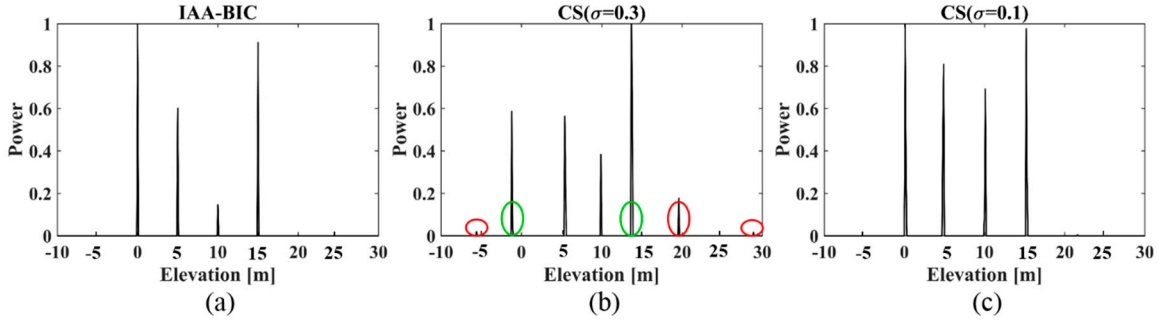

Figure 2. The sparse elevation profiles reconstructed by the tomographic estimators with single-look: (**a**) IAA-BIC; (**b**) CS with the hyperparameter at 0.3 ($\sigma = 0.3$); (**c**) CS with the hyperparameter at 0.1 ($\sigma = 0.1$).

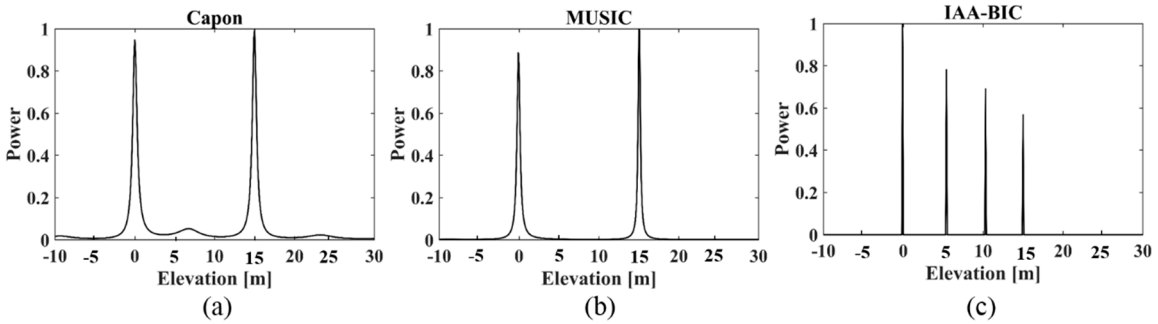

Figure 3. The elevation profiles reconstructed by the tomographic estimators with 25 looks: (**a**) Capon; (**b**) MUSIC; (**c**) IAA-BIC.

On the basis of the above analysis, the IAA-BIC estimator can work well for both coherent and distributed sources. Furthermore, it can also obtain a good performance in the case of single-look, which can maintain the spatial resolution. In addition, it can obtain a sparse estimation without requiring any difficult selection of hyperparameter, avoiding considerable computational consumption.

4. Real-Data Experiment and Results

A real spaceborne SAR dataset was applied in TomoSAR to retrieve the three-dimensional structure of an urban infrastructure; this was performed to investigate the feasibility and effectiveness of the IAA-BIC method in comparison to in-situ measurement.

4.1. Study Area and Dataset

The study area is located at the city of Wuhan, Hubei province, China (see Figure 4). Wuhan (113°41′ E–115°05′ E, 29°58′ N–31°22′ N) is the capital of Hubei province and the largest metropolis in central china, with an area of 8494.41 km^2. The topography of the study area is relatively flat with many high-rise buildings.

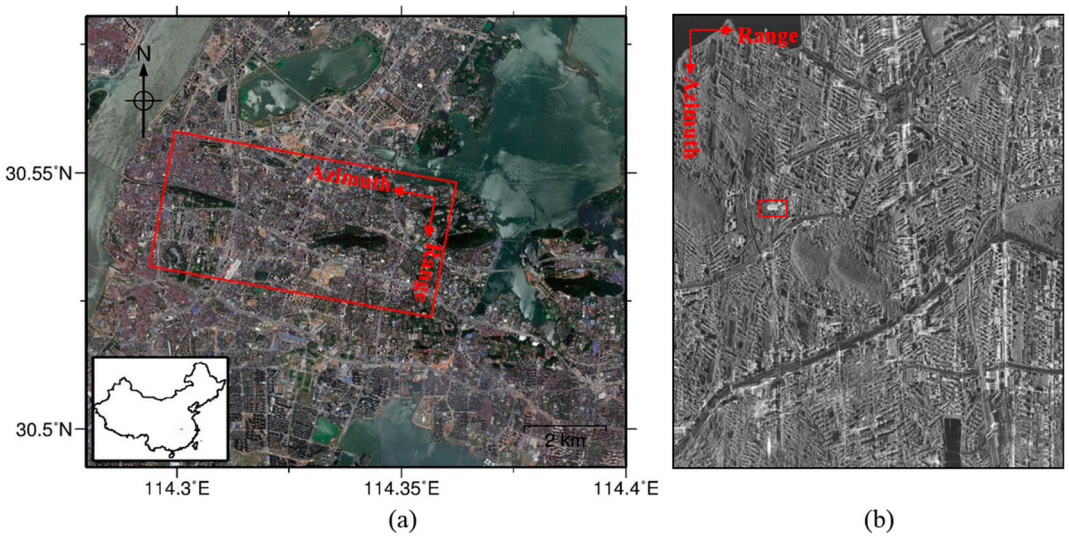

Figure 4. (**a**) Geographic location of the study area overlaid on an optical image. The red rectangle represents the footprint of the selected SAR images. (**b**) The intensity map of the determined master SAR image acquired on 15 June 2015.

Table 1. Parameters of the TerraSAR-X dataset.

Polarization Mode	Wavelength (cm)	Incidence Angle	Slant Range (m)	Azimuth Spacing (m)	Range Spacing (m)
HH	3.10	31.003°	589,061.4613	0.17	0.45

We collected nine TerraSAR-X very high spatial resolution staring-mode images spanning from 28 June 2014, to 10 January 2016, over this study area. The parameters of the dataset are listed in Table 1. The image acquired on 15 June 2015 was considered the master image. The spatial perpendicular baselines with respect to the master track are shown in Figure 5.

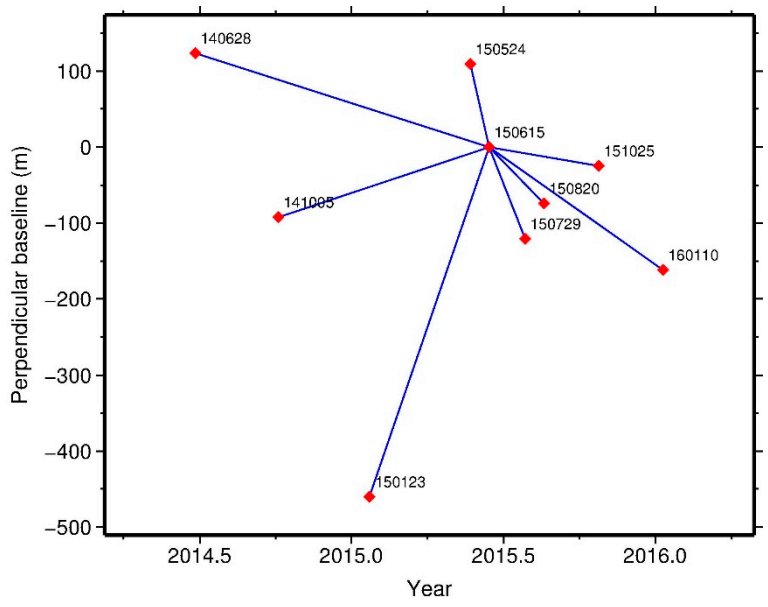

Figure 5. The spatial perpendicular baselines of all the InSAR pairs.

4.2. Results and Analysis

The Hubei Science and Technology Venture building (the red circle shown in Figure 4b) was chosen from the study area as a test building for tomographic focusing. This building is located beside the overpass at Luoshi Road (Figure 6a). The overpass appears to go through the selected building on the geocoded SAR intensity map (Figure 6b), which suggests that layover has taken place. Accordingly, it is expected to generate different scattering mechanisms.

According to multiple field-survey measurements taken at different angles with a hand-held laser rangefinder, the building is 99 m high (26 floors). From the illumination direction map (Figure 7b), only about one-third of the Hubei Science and Technology Venture building can be imaged on the SAR images. The building features a glass wall (see Figure 7c). Given the smooth surface of the glass wall, specular reflection occurs, and little echo can be received. Thus, four building walls and three gaps are seen in the intensity map (Figure 7a).

An azimuth profile (the red line shown in Figure 7a) was selected as an example to undertake tomographic focusing, which corresponds to the red polyline in Figure 7b. Figure 8 presents tomograms of this profile estimated by the IAA-BIC estimator with single-look and multi-look (the number of looks $L = 25$). The tomogram segments clearly show different scattering contribution patterns. The segment near 25 m along the height corresponds to the building wall. The tomogram segments circled by the yellow ellipses represent the ground scattering contribution. The multi-look IAA-BIC detected fewer ground scatterers than the single-look IAA-BIC. Furthermore, there is no ground contribution between the two yellow circles in Figure 8b, a result of the wall scattering which dominates this area as well as the weak ground scattering. When the IAA-BIC estimator was applied to multi-look, it regarded the ground scattering source as noise and suppressed it. Moreover, there were two scatterers for the tomogram segment marked by the red circles, which resulted from the layover caused by the test building and the overpass on Luoshi Road. This indicates that the IAA-BIC estimator can discriminate two coherent scatterers. These two scatterers were considered as coherent scatterers because the distributed scatterers presented a very poor performance in TomoSAR with temporal decorrelation. In our case, the temporal decorrelation cannot be ignored, due to the significant time taken for the acquisitions. In addition, the IAA-BIC estimator showed a similar performance with single-look and multi-look. Although the tomogram of multi-look is more stable than that of single-look, the high azimuth-range resolution is greatly reduced, which is undesirable.

We then obtained the tomograms in each resolution cell and estimated their heights. Figure 9 shows the reconstructed and color-coded elevation of the test building from the IAA-BIC estimator with single-look and multi-look, respectively, visualized in two layers and overlaid with the intensity. The first layer is the height of scatterers with a high reflectivity power, and the second layer is derived from the scatterers with a low reflectivity power. This clearly shows that IAA-BIC obtains a similar height estimation with both single-look and multi-look. However, slightly more bias existed in the single-look results. For the first layer, the wall scatterers were the main contribution; their height varies from low to high, which is consistent with the change trend from the ground to the roof. As for the second layer, the overpass largely contributed to the scatterers.



Figure 6. (**a**) Location of the Hubei Science and Technology Venture building on a Google Earth map. (**b**) Location of the Hubei Science and Technology Venture building on the geocoded TerraSAR-X master image.

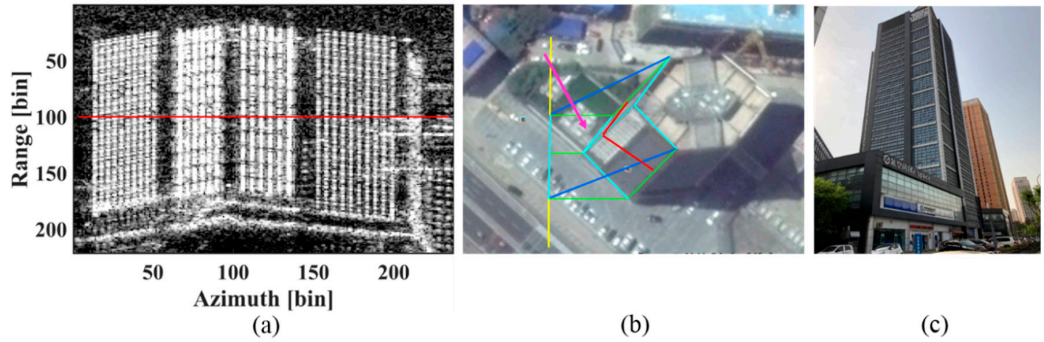

Figure 7. (**a**) The selected azimuth profile on the SAR intensity map of the Hubei Science and Technology Venture building. (**b**) The SAR illumination direction for the Hubei Science and Technology Venture building. (**c**) The Hubei Science and Technology Venture building.

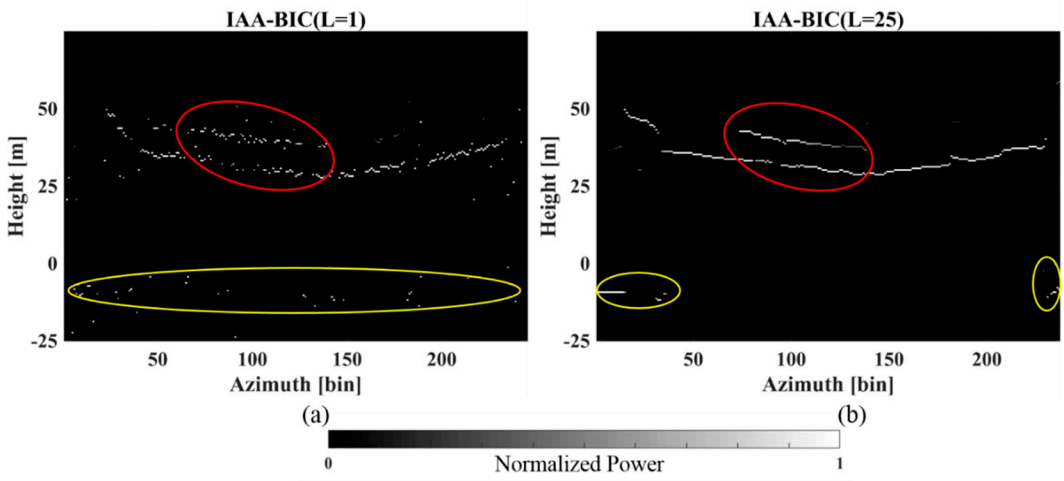

Figure 8. The tomograms estimated by the IAA-BIC method with different looks: (**a**) single-look (L = 1); (**b**) multi-look (L = 25).

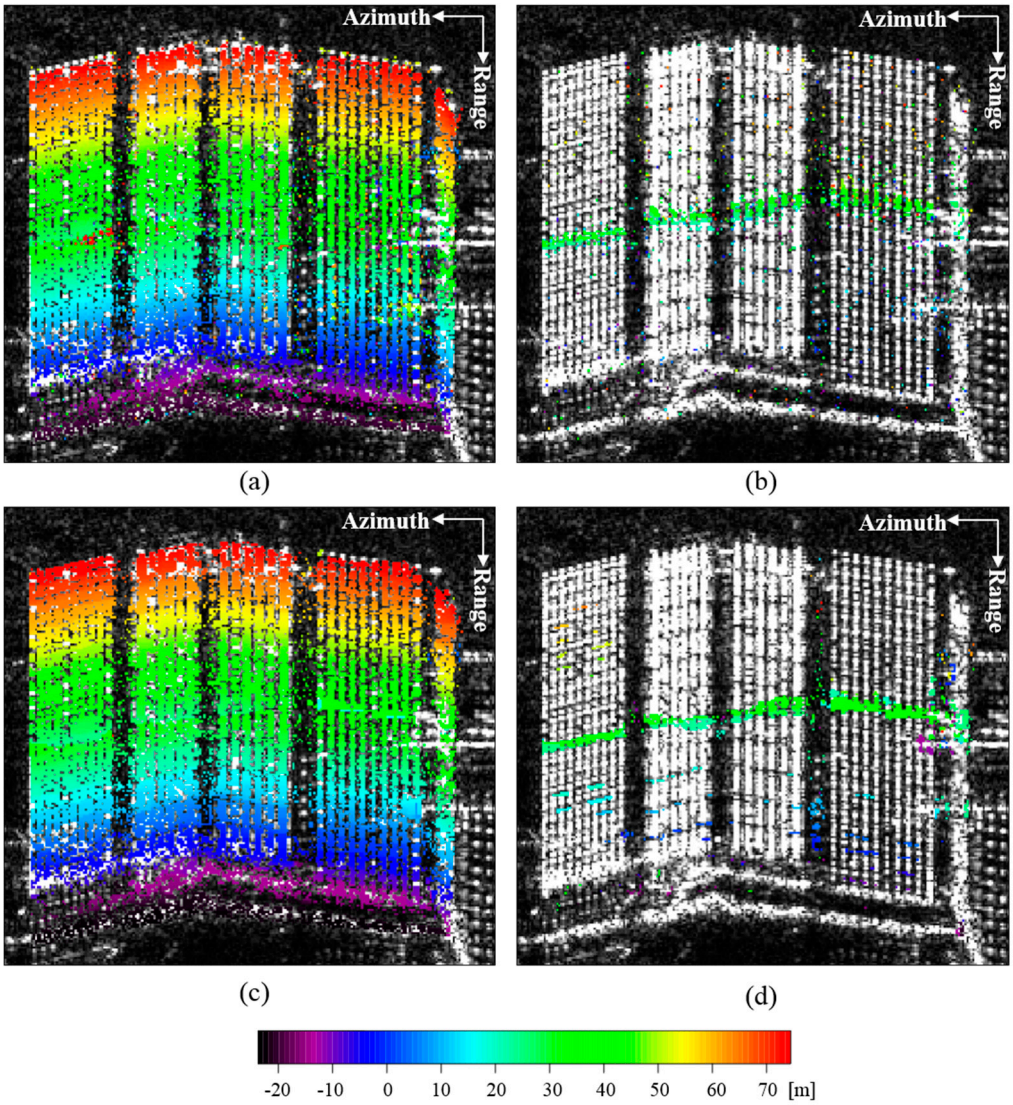

Figure 9. Reconstructed and color-coded elevation of the test building overlaid with intensity, visualized in two layers: (**a**) first layer estimated by IAA-BIC with single-look; (**b**) second layer estimated by IAA-BIC with single-look; (**c**) first layer estimated by IAA-BIC with multi-look; (**d**) second layer estimated by IAA-BIC with multi-look.

Finally, the building's height could be obtained from the position difference between the roof and the ground along the height. Table 2 gives the building's height estimation and the corresponding evaluation for the single-look and multi-look, respectively. This suggests that IAA-BIC obtains a high estimation accuracy, relative to the real height, with both the single-look (relative error 0.76/99 = 1%) and multi-look (relative error 3.26/99 = 4%). This indicates that the IAA-BIC method was highly reliable in this study case. Furthermore, the single-look version obtained a much smaller estimation error than the multi-look version because the single-look version could maintain the inherent scale of the urban infrastructure. In contrast, the multi-look version averaged all the scales in the estimation window, degrading the spatial resolution of the inversed 3-D structure map in both the azimuth and slant-range directions. This also accounts for why we have developed and recommend the single-look tomographic method for use in urban areas.

Table 2. The absolute building height and estimation error obtained by IAA-BIC with single-look and multi-look.

IAA-BIC	Single-Look	Multi-Look
Building height (m)	98.24	95.74
Estimation error (m)	0.76	3.26

The above analysis confirms that the IAA-BIC method is a reliable way to obtain the three-dimensional structure of urban infrastructures, and it can work well even with single-look. Although the results of the single-look version contained more bias than those of the multi-look version, it retrieved a higher estimation accuracy.

5. Discussion

To further demonstrate the performance of the proposed IAA-BIC method, the classical nonparametric spectral estimation method known as Capon, the classical parametric spectral estimation method known as MUSIC, and the CS estimator were also used to undertake tomographic focusing at the same azimuth profile (the red dashed line segment in the test zone, shown in Figure 7a). The same parameters (estimation window, height range, and height sample interval) were used in Capon, MUSIC, and the CS estimator.

5.1. Comparison between IAA-BIC and Capon

5.1.1. Theoretical Analysis

Capon, which is also known as "adaptive beamforming", determines the weight vector by minimizing the output power, subject to the constraint that the signal of interest is undistorted. For the imaging model (Equation (3)), when the true covariance matrix R and a_d are known, Capon can be formulated as [12,41]:

$$\min_{P} P^* RP \; s.t. \; P^* a_d = 1 \tag{16}$$

The solution to the optimization problem is given by [12,41]:

$$w_{opt} = \frac{R^{-1} a_d}{a_d^* R^{-1} a_d} \tag{17}$$

The spectrum of Capon is expressed as [12,41]:

$$\hat{P}_{\text{Capon}} = w_{opt}^* R w_{opt} = \frac{1}{a_d^* R^{-1} a_d} \tag{18}$$

Note that the iterative equations of IAA-BIC are the same form as (17) and the denominator of (18), respectively. In practice, the covariance matrix R in Capon is estimated from the sample covariance matrix with $\hat{R} = \frac{1}{L}\sum_{l=1}^{L} y(l)y(l)^*$. However, in IAA-BIC, the covariance matrix R is obtained from the estimates of the previous iteration. Through this iterative process, the estimates are the closest to their true values, which is impossible for Capon. Accordingly, IAA-BIC can obtain a better performance than Capon.

5.1.2. Experimental Analysis

Figure 10 shows the tomograms estimated by Capon and IAA-BIC with multi-look (L = 25). For the segment circled by the red ellipse, IAA-BIC successfully separated two coherent scatterers, but Capon failed to discriminate them. Moreover, Capon obtained a biased estimation for the segment marked by the yellow circles where the wall contribution dominates. These results indicate that IAA-BIC can obtain a better elevation resolution than Capon.

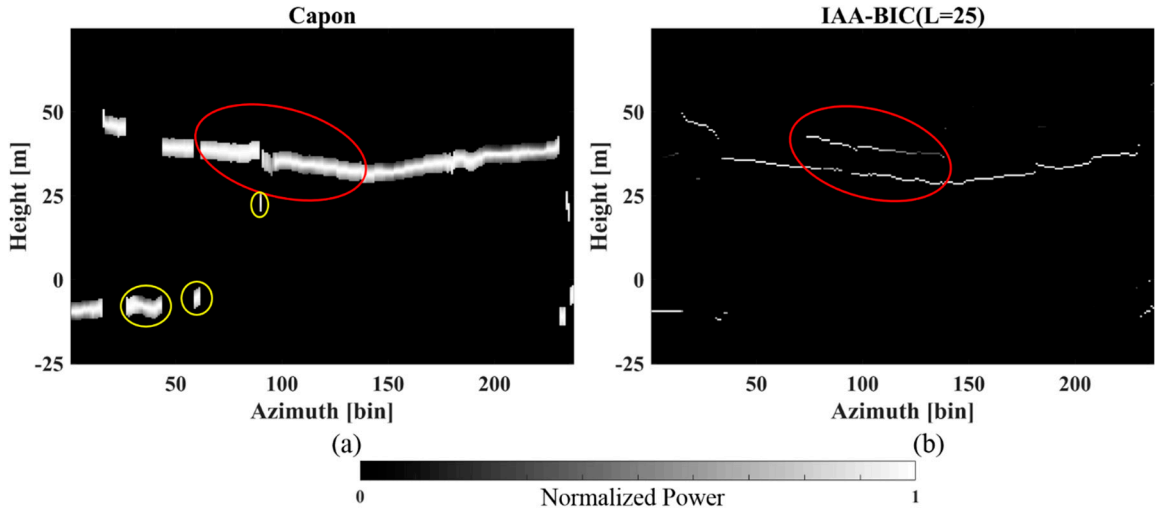

Figure 10. The tomograms estimated by the two estimators with multi-look: (**a**) Capon; (**b**) IAA-BIC.

5.2. Comparison between IAA-BIC and MUSIC

5.2.1. Theoretical Analysis

MUSIC is a subspace-based technique which decomposes the covariance matrix R into its eigenvalues and eigenvectors and then analyzes their properties. The MUSIC spectrum is obtained as [14,41]:

$$\hat{P}_{\text{music}} = \frac{1}{a_d^H G G^H a_d} \tag{19}$$

where G is the matrix of the noise subspace, which is determined by the N-K eigenvectors corresponding to the N-K smallest eigenvalues of the covariance matrix R. K is the number of scatterers in one resolution, which is the required prior information.

The estimation of covariance matrix R directly influences the performance of MUSIC. Similar to Capon, the covariance matrix R in MUSIC is also estimated by the sample covariance matrix $\hat{R}$. This means that MUSIC cannot achieve the closest estimation of covariance matrix R. Moreover, when different scatterer numbers K are inputted, MUSIC shows a different performance and is sensitive to the model error. However, IAA-BIC does not require any prior information and can obtain the closest estimate of the covariance matrix. Thus, IAA-BIC performs better than MUSIC.

5.2.2. Experimental Analysis

In this part, we assumed that the number of scatterers for the MUSIC estimator was two. The tomograms of the azimuth profile were estimated by MUSIC and IAA-BIC with multi-look, as shown in Figure 11. The IAA-BIC could successfully discriminate two coherent scatterers in the region circled by the red ellipses, but MUSIC failed to do so. This suggests that IAA can obtain a good elevation resolution in the case of coherent sources.

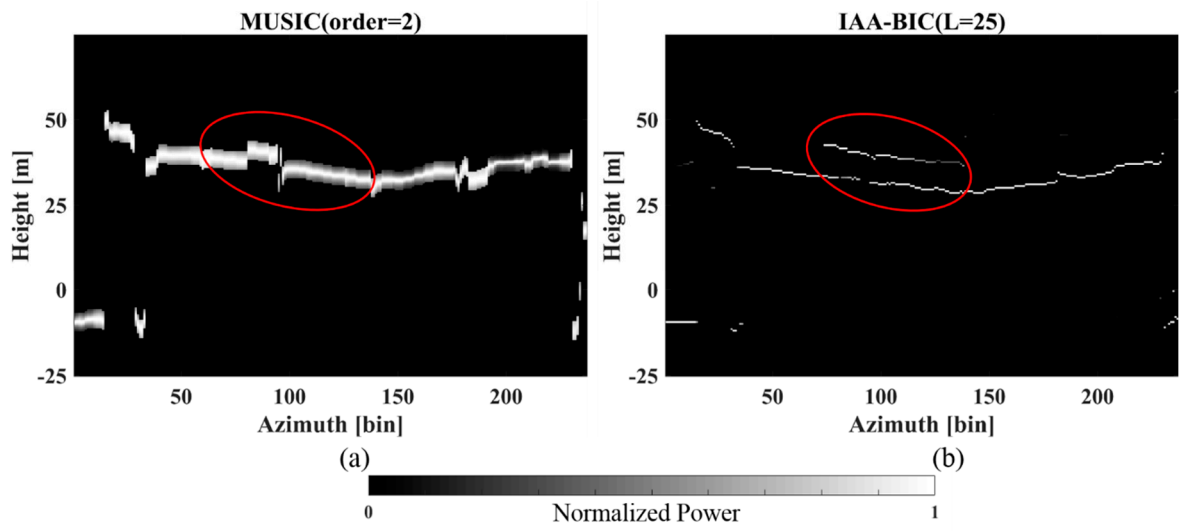

Figure 11. The tomograms estimated by the two estimators with multi-look: (**a**) MUSIC; (**b**) IAA-BIC.

5.3. Comparison between IAA-BIC and CS

5.3.1. Comparison of Estimation Accuracy

The two sparse TomoSAR estimators (IAA-BIC and CS) were applied to obtain the tomogram of the azimuth profile with single-look (see Figure 12). For details of the CS algorithm, we refer the reader to studies by Zhu et al. [19] and Budillon et al. [30]. Notably, the two estimators obtained tomograms that ere the same apart from the section outlined by the red circles, in which IAA-BIC recognized slightly more scatterers than CS. This is because IAA-BIC is completely data adaptive for every pixel, while CS relies on the hyperparameter, which is upper bound on the noise level. Accordingly, it is difficult for a selected hyperparameter to meet the noise level in every resolution cell in practice.

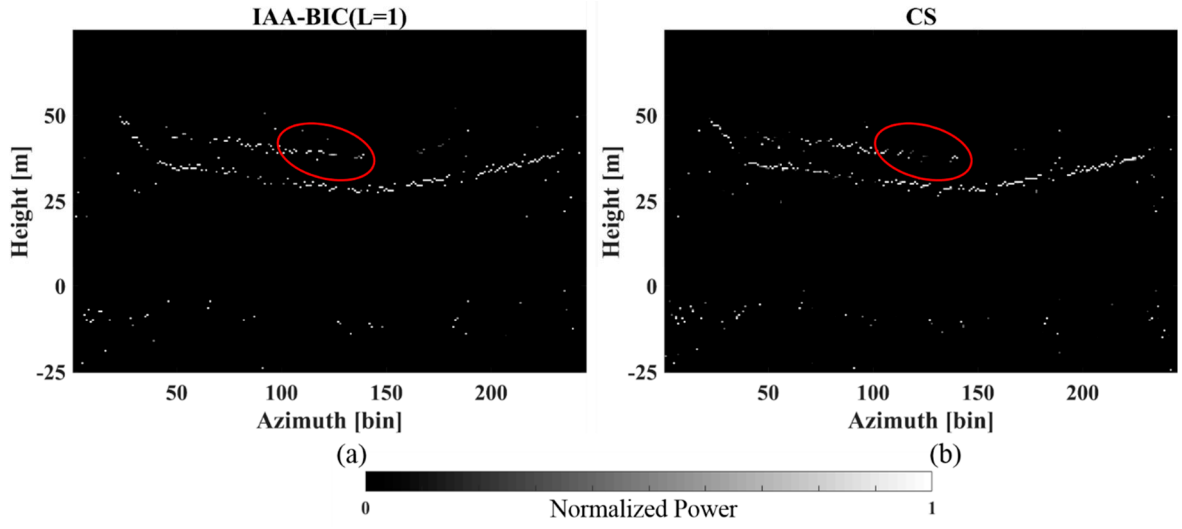

Figure 12. The tomograms estimated by the two estimators with single-look: (**a**) IAA-BIC; (**b**) CS.

5.3.2. Comparison of Computational Time Consumption

In this experiment, the performance of IAA-BIC was not significantly improved after about 15 iterations, which conforms to the empirical experience described in Yardibi et al. [33]. For this profile, IAA took 186 s to obtain the tomogram.

For the CS estimator, there is theoretically an optimal hyperparameter to make the result optimal, but there is no accepted method to select this optimal value at present. In general, if this value is too small, it can lead to overfitting, whereas a too large value can lead to underfitting. The selection of the hyperparameter by the user is critical, and, to obtain a good result, it requires repeated attempts. For this tomogram estimation, the CS estimator took approximately one and half hours, which is 30 times that of IAA-BIC.

The above analysis shows that IAA-BIC has several advantages: (1) it can obtain a good resolution for coherent scatterers; (2) it is a completely adaptive approach, without requiring any hyperparameter, avoiding the considerable computational burden; and (3) it can also obtain a good performance with single-look, maintaining the spatial resolution.

6. Conclusions

In this paper, we have proposed the IAA-BIC TomoSAR method for application in urban areas. This is an iterative adaptive approach with a model-order selection tool based on BIC, allowing sparse point estimation. IAA-BIC is based on weighted least squares estimation. The IAA-BIC estimator allows reflectivity profile reconstruction in urban areas along the elevation direction and can discriminate different scatterers with a high degree of accuracy.

To demonstrate the advantages of IAA-BIC, two sets of simulated experiments were carried out. The results showed that the IAA-BIC TomoSAR method has three main advantages: (1) IAA-BIC can successfully separate coherent and distributed scatterers; (2) IAA-BIC can obtain a high elevation resolution, without requiring any difficult selection of hyperparameter; and (3) IAA-BIC works well not only with multi-look but also single-look. Moreover, about nine very high spatial resolution TerraSAR-X images were used to demonstrate the feasibility and effectiveness of the IAA-BIC estimator. The results showed that IAA-BIC could successfully separate two coherent scatterers and could obtain a reliable three-dimensional structure for the Hubei Science and Technology Venture building in Wuhan, China. The height estimation accuracy of this building was about 1% and 4% relative to its real height for the single-look and multi-look, respectively. Although the IAA-BIC results of the single-look version contain slightly more bias than the results of the multi-look version, it can obtain a higher estimation accuracy while maintaining the spatial resolution. In addition, the typical TomoSAR estimators of Capon, MUSIC, and CS were applied in a comparison with IAA-BIC. In terms of the theoretical analysis and experimental analysis, IAA-BIC obtained a higher resolution than Capon and MUSIC. In comparison to CS, IAA-BIC performed slightly better because it is data adaptive for every pixel cell, whereas CS depends on the hyperparameter.

In conclusion, IAA-BIC can obtain a high elevation resolution to retrieve the three-dimensional structure of urban objects, without sacrificing the spatial resolution or requiring any prior information. Meanwhile, the user is not required to make any difficult selection of hyperparameter.

In our further work, we will focus on an extension of IAA-BIC from a TomoSAR application to a differential TomoSAR (D-TomoSAR) application. Admittedly, TomoSAR is a good way to discriminate different scatterers within a resolution cell, thereby providing the height information. However, it cannot obtain the deformation of each scatterer along the elevation. D-TomoSAR makes this possible because it is not only aimed at reflectivity and height estimation but also deformation estimates.

Author Contributions: X.P. conceived the idea, designed and performed the experiments, produced the results, and drafted the manuscript. C.W. acquired the datasets. X.L. contributed to discuss with the idea and results. Y.D., H.F., Z.Y. and Q.X. contributed to the discussion of the results and revision of the article. All authors reviewed and approved the manuscript.

Funding: This research was funded by the National Natural Science Foundation of China (No. 41571360, No. 41371335, No. 41671356, and No. 41531068) and the Natural Science Foundation of Hunan Province, China (No. 2016JJ2141).

Acknowledgments: The TerraSAR-X datasets were provided by the DLR (No. MTH2350 and LAN2235).

Conflicts of Interest: The authors declare no conflict of interest.

References

1. Roth, A. TerraSAR-X: A new perspective for scientific use of high resolution spaceborne SAR data. In Proceedings of the 2nd GRSS/ISPRS Joint Workshop on Remote Sensing and Data Fusion over Urban Areas, Berlin, Germany, 22–23 May 2003.
2. Krieger, G.; Moreira, A.; Fiedler, H.; Hajnsek, I. TanDEM-X: A satellite formation for high-resolution SAR interferometry. *Trans. Geosci. Remote Sens.* **2007**, *45*, 3317–3341. [CrossRef]
3. Covello, F.; Battazza, F.; Coletta, A.; Lopinto, E.; Fiorentino, C.; Pietranera, L.; Valentini, G.; Zoffoli, S. COSMO-SkyMed an existing opportunity for observing the Earth. *J. Geodyn.* **2010**, *49*, 171–180. [CrossRef]
4. Yang, M.; Jiang, Y.; Liao, M.; Wang, H. Application of TomoSAR in urban deformation surveillance. *Shanghai Land Resour.* **2013**, *34*, 7–11.
5. Pasquali, P.; Prati, C.; Rocca, F. A 3-D SAR Experiment with EMSL Data. In Proceedings of the 1995 International Geoscience and Remote Sensing Symposium (IGARSS'95), Florence, Italy, 10–14 July 1995; pp. 784–786.
6. Reigber, A.; Moreira, A. First demonstration of airborne SAR tomography using multibaseline L-band data. *IEEE Trans. Geosci. Remote Sens.* **2000**, *38*, 2142–2152. [CrossRef]
7. Gini, F.; Lombardini, F.; Montannari, M. Layover solution in multibaseline SAR interferometry. *IEEE Trans. Aerosp. Electron. Syst.* **2005**, *20*, 71–93. [CrossRef]
8. She, Z.; Gray, D.; Bogner, R.; Homer, J. Three-dimensional SAR imaging via multiple pass processing. In Proceedings of the 1995 International Geoscience and Remote Sensing Symposium (IGARSS'95), Florance, Italy, 28 June–2 July 1995; Volume 5, pp. 2389–2391.
9. Lombardini, F.; Reigber, A. Adaptive Spectral Estimation for Multi-baseline SAR Tomography with Airborne L-band Data. In Proceedings of the 2003 IEEE International Geoscience and Remote Sensing Symposium (IGARSS), Toulouse, France, 21–25 July 2003; Volume 3, pp. 2014–2016.
10. Fornaro, G.; Serafino, F.; Soldovieri, F. Three-dimensional Focusing with Multipass SAR Data. *IEEE Trans. Geosci. Remote Sens.* **2003**, *41*, 507–517. [CrossRef]
11. Lombardini, F.; Gini, F.; Matteucci, P. Application of array processing techniques to multibaseline InSAR for layover solution. In Proceedings of the 2001 IEEE Radar Conference, Atlanta, GA, USA, 3 May 2001; pp. 210–215.
12. Kumar, S.; Joshi, S.K.; Govil, H. Spaceborne PolSAR Tomography for Forest Height Retrieval. *IEEE J. Sel. Top. Appl. Earth Obs. Remote Sens.* **2017**, *10*, 5175–5185. [CrossRef]
13. Gini, F.; Lombardini, F. Multilook APES for Multi-baseline SAR Interferometry. *IEEE Trans. Signal Proc.* **2002**, *50*, 1800–1803. [CrossRef]
14. Sauer, S.; Ferro-Famil, L.; Reigber, A.; Pottier, E. Three-dimensional imaging and scattering mechanism estimation over urban scenes using dual-baseline polarimetric InSAR observations at L-band. *IEEE Trans. Geosci. Remote Sens.* **2011**, *49*, 4616–4629. [CrossRef]
15. Huang, Y.; Ferro-Famil, L. 3D characterization of buildings in a dense urban environment using L-band PolInSAR data with irregular baselines. In Proceedings of the 2009 IEEE International Geoscience and Remote Sensing Symposium (IGARSS), Cape Town, South Africa, 12–17 July 2009; Volume 3, pp. 29–32.
16. Huang, Y.; Ferro-Famil, L.; Reigber, A. Under-foliage Object Imaging Using SAR Tomography and Polarimetric Spectral Estimators. *IEEE Trans. Geosci. Remote Sens.* **2012**, *50*, 2213–2225. [CrossRef]
17. Wei, L.; Balz, T.; Liao, M.; Zhang, L. A Novel Fast Approach for SAR Tomography: Two step iterative Shrinkage/Thresholding. *IEEE Geosci. Remote Sens. Lett.* **2015**, *12*, 1377–1381.
18. Tebaldini, S. Algebraic Synthesis of Forest Scenarios from Multi-baseline PolInSAR Data. *IEEE Trans. Geosci. Remote Sens.* **2009**, *47*, 4132–4142. [CrossRef]
19. Zhu, X.X.; Bamler, R. Very High Resolution Spaceborne SAR Tomography in Urban Environment. *IEEE Trans. Geosci. Remote Sens.* **2010**, *48*, 4296–4308. [CrossRef]
20. Pardini, M.; Papathanassiou, K. On the Estimation of Ground and Volume Polarimetric Covariances in Forest Scenarios with SAR Tomography. *IEEE Geosci. Remote Sens. Lett.* **2017**, *14*, 1860–1864. [CrossRef]
21. Zhu, X.X.; Bamler, R. Tomographic SAR Inversion by L1-Norm Regularization—The Compressive Sensing Approach. *IEEE Trans. Geosci. Remote Sens.* **2010**, *48*, 3839–3846. [CrossRef]

22. Zhu, X.X.; Bamler, R. Super-Resolution Power and Robustness of Compressive Sensing for Spectral Estimation with Application to Spaceborne Tomographic SAR. *IEEE Trans. Geosci. Remote Sens.* **2011**, *50*, 247–258. [CrossRef]
23. Sun, X.; Yu, A.; Dong, Z.; Liang, D. Three-Dimensional SAR Focusing via Compressive Sensing: The Case Study of Angel Stadium. *IEEE Geosci. Remote Sens. Lett.* **2012**, *9*, 759–763.
24. Zhu, X.X.; Bamler, R. Super Resolution SAR Tomography for Multi-dimensional Imaging of Urban Areas: Compressive Sensing-based TomoSAR Inversion. *IEEE Signal Proc. Mag.* **2014**, *31*, 51–58. [CrossRef]
25. Biondi, F. SAR Tomography Optimization by Interior Point Method via Atomic Decomposition—The Convex Optimization Approach. In Proceedings of the 2014 IEEE International Geoscience and Remote Sensing Symposium (IGRASS), Quebec City, QC, Canada, 13–18 July 2014; pp. 1879–1882.
26. Liang, L.; Guo, H.; Li, X. Three-Dimensional Structural Parameter Inversion of Buildings by Distributed Compressive Sensing-Based Polarimetric SAR Tomography Using a Small Number of Baselines. *IEEE J. Sel. Top. Appl. Res. Obs. Remote Sens.* **2014**, *7*, 4218–4230. [CrossRef]
27. Ma, P.F.; Lin, H.; Lan, H.X.; Chen, F.L. On the Performance of Reweighted L1 Minimization for Tomographic SAR Imaging. *IEEE Geosci. Remote Sens. Lett.* **2015**, *12*, 895–899. [CrossRef]
28. Li, X.; Liang, L.; Guo, H. Compressive Sensing for Multibaseline Polarimetric SAR Tomography of Forested Areas. *IEEE Trans. Geosci. Remote Sens.* **2016**, *54*, 153–166. [CrossRef]
29. Liang, L.; Li, X.; Ferro-Famil, L.; Guo, H.; Zhang, L.; Wu, W. Urban Area Tomography Using a Sparse Representation Based Two-Dimensional Spectral Analysis Technique. *Remote Sens.* **2018**, *10*, 109. [CrossRef]
30. Budillon, A.; Evangelista, A.; Schirinzi, G. Three dimensional SAR focusing from multi-pass signals using compressive sampling. *IEEE Trans. Geosci. Remote Sens.* **2011**, *49*, 488–499. [CrossRef]
31. Budillon, A.; Evangelista, A.; Schirinzi, G. SAR tomography from sparse samples. In Proceedings of the 2009 IEEE International Geoscience and Remote Sensing Symposium (IGARSS), Cape Town, South Africa, 12–17 July 2009; Volume 4, pp. 865–868.
32. Cazcarra-Bes, V.; Tello-Alonso, M.; Fisher, R.; Heym, M.; Papathanassiou, K. Monitoring of Forest Structure Dynamics by Means of L-Band SAR Tomography. *Remote Sens.* **2017**, *9*, 1229. [CrossRef]
33. Yardibi, T.; Li, J.; Stoica, P.; Xue, M.; Baggeroer, A.B. Source Localization and Sensing: A Nonparametric Iterative Adaptive Approach Based on Weighted Least Squares. *IEEE Trans. Aerosp. Electron. Syst.* **2010**, *46*, 425–443. [CrossRef]
34. Du, L.; Yardibi, T.; Li, J.; Stoica, P. Review of user parameter-free robust adaptive beamforming algorithms. *Dig. Signal Proc.* **2009**, *19*, 567–582. [CrossRef]
35. Schwarz, G. Estimating the dimension of a model. *Ann. Stat.* **1978**, *6*, 461–464. [CrossRef]
36. Stoica, P.; Selen, Y. Model-order selection: A review of information criterion rules. *IEEE Signal Proc. Mag.* **2004**, *21*, 36–47. [CrossRef]
37. Lombardini, F.; Gini, F. Model order selection in multi-baseline interferometric radar systems. *EURASIP J. Appl. Signal Proc.* **2005**, *20*, 3206–3219. [CrossRef]
38. Wax, M.; Kailath, T. Detection of signals by information theoretic criteria. *IEEE Trans. Acoust. Speech Signal Proc.* **1985**, *33*, 387–392. [CrossRef]
39. Wax, M.; Ziskind, I. Detection and localization of multiple sources via the stochastic signal model. *IEEE Trans. Signal Proc.* **1991**, *39*, 2450–2456. [CrossRef]
40. Grant, M.; Boyd, S. *CVX: MATLAB Software for Disciplined Convex Programming*, version 2.1; Tech. Rep.; 2014. Available online: http://cvxr.com/cvx (accessed on 10 June 2015).
41. Stoica, P.; Moses, R.L. *Spectral Analysis of Signals*; Prentice-Hall: Upper Saddle River, NJ, USA, 2005.



© 2018 by the authors. Licensee MDPI, Basel, Switzerland. This article is an open access article distributed under the terms and conditions of the Creative Commons Attribution (CC BY) license (http://creativecommons.org/licenses/by/4.0/).